Article

aeroacoustics

International Journal of Aeroacoustics
2016, Vol. 15(8) 734–756

DOI: 10.1177/1475472X16672322
jae.sagepub.com
SAGE

Numerical analysis of aerodynamic noise mitigation via leading edge serrations for a rod–airfoil configuration

Bharat Raj Agrawal and Anupam Sharma

Abstract

Noise produced by aerodynamic interaction between a circular cylinder (rod) and an airfoil in a tandem arrangement is investigated numerically using incompressible large eddy simulations. Quasi-periodic shedding from the rod and the resulting wake impinges on the airfoil to produce unsteady loads on the two geometries. These unsteady loads act as sources of aerodynamic sound and the sound radiates to the far-field with a dipole directivity. The airfoil is set at zero angle of attack for the simulations and the Reynolds number based on the rod diameter is $Re_d = 48\,\mathrm{K}$. Comparisons with experimental measurements are made for (a) mean and root mean square surface pressure on the rod, (b) profiles of mean and root mean square streamwise velocity in the rod wake, (c) velocity spectra in the near field, and (d) far-field pressure spectra. Curle's acoustic analogy is used with the airfoil surface pressure data from the simulations to predict the far-field sound. An improved correction based on observed spanwise coherence is used to account for the difference in span lengths between the experiments and the simulations. Good agreement with data is observed for the near-field aerodynamics and the far-field sound predictions. The straight leading edge airfoil is then replaced with a test airfoil with a serrated leading edge geometry while maintaining the mean chord. This new configuration is also analyzed numerically and found to give a substantial reduction in the far-field noise spectra in the mid- to high-frequency range. Source diagnostics show that the serrations reduce unsteady loading on the airfoil, reduce coherence along the span, and increase spanwise phase variation, all of which contribute to noise reduction.

Keywords

Rod-airfoil interaction, leading edge serrations, large eddy simulations

Date received: 31 May 2016; accepted: 10 September 2016

Department of Aerospace Engineering, Iowa State University, Ames, IA, USA

Corresponding author:
Anupam Sharma, Department of Aerospace Engineering, Iowa State University, 2271 Howe Hall, Ames, IA 50011, USA.
Email: sharma@iastate.edu

Introduction

Aerodynamic noise is a by-product of most engineering machines, e.g., aircraft, gas turbines, and household fans. Noise can be either tonal, in which case the acoustic energy is limited to a few discrete tones, or broadband, in which case the energy is spread across a wide range of frequencies. Flow turbulence is often the source of broadband aerodynamic noise. The wide range of time scales of turbulent eddies results in noise that is produced over a wide range of frequencies. Until recently, such broadband noise sources were estimated using approximate models for the flow turbulence energy spectrum, which is typically scaled using the turbulence kinetic energy and the integral length scale in the problem. These parameters are obtained by solving the Reynolds-averaged Navier–Stokes (RANS) equations, which are computationally much less expensive to solve than simulations that resolve every minute detail in the flow (e.g., direct numerical simulations). Large-scale computing has now become available to researchers, which allows direct computation of the full range of length and time scales important for sound generation and propagation. Such an approach gets rid of the modeling assumptions required in simpler models and thus provides more accurate predictions. The large eddy simulations (LES) technique is one such computational method that is becoming increasingly popular for noise prediction from engineering machines. Noise computation of a model engineering problem is presented here using LES.

The model problem is to compute the noise produced due to the aerodynamic interaction between a circular cylinder (rod) and an airfoil (see Figure 1). The rod is placed upstream (in tandem) of the NACA 0012 airfoil. Wake/vorticity shed from the rod convects with the flow and impinges on the downstream airfoil. This impingement (oftentimes characterized by the upwash on the airfoil) produces unsteady lift on the airfoil, which radiates as noise, as seen in Figure 1(b). At $Re_d = 48{,}000$, quasi-periodic vortex shedding is expected behind the rod, which gives rise to tones at the vortex shedding frequency (Strouhal number, $St \sim 0.19$) and its harmonics. In addition, the turbulence in the vortices and the wake generates broadband noise. The resulting noise spectrum has a broadband "floor" above which tones with broadened peaks are observed at the shedding frequency and its harmonics. This problem was experimentally investigated by Jacob et al.[1] and has been widely used by various researchers to benchmark their codes' capability and accuracy. The measurements[1] include

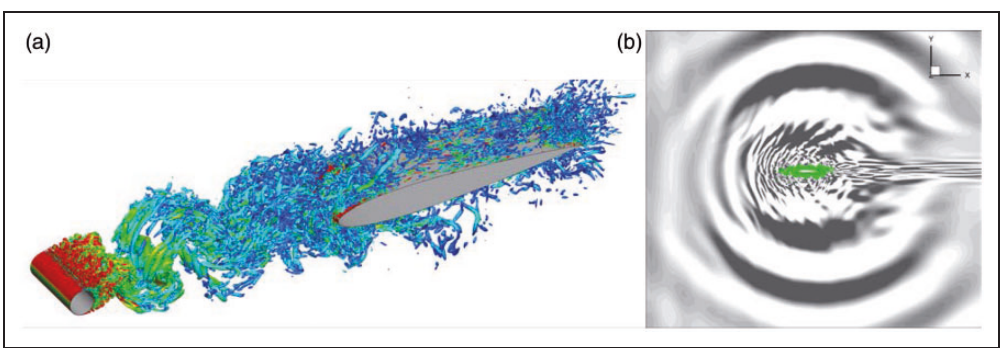

Figure 1. Snapshots from a *compressible* LES simulation by Agrawal and Sharma[2] for the rod–airfoil problem: (a) hydrodynamic flow field illustrated using iso-surfaces of Q-criterion ($Q = 25$) with contours colored by the magnitude of density gradient, and (b) far-field acoustics shown using fluid dilatation, $\nabla.\mathbf{v}$.

wake and boundary layer profiles (mean and turbulent statistics), near-field velocity spectra, and far-field noise.

Literature review

A number of numerical studies have been carried out for the specific rod–airfoil configuration considered here. Casalino et al.[3] was the first to numerically investigate this problem using unsteady RANS simulations. The simulations were two-dimensional (2D) and three-dimensional (3D) effects on noise were modeled using a statistical model coupled with the Ffowcs Williams–Hawkings (FW–H) acoustic analogy. The statistical model was calibrated using the experimental data.

The LES technique has also been used to model this problem. Boudet et al.[4] reported the first LES computations for this benchmark problem. It used finite-volume, compressible LES on multi-block structured grids. Far-field noise was obtained by coupling the near-field data with a permeable FW–H solver. Berland et al.[5] performed direct noise computations using high-order, compressible LES on overset structured grids. They also investigated the effect on noise of varying the spacing between the rod and the airfoil. Eltaweel and Wang[6] used an incompressible LES solver coupled with a boundary element method to predict far-field noise. An unstructured mesh composed of 22.3 million cells was used. Their results showed very good agreement with data for near-field flow measurements as well as far-field acoustics.

Giret et al.[7,8] used a compressible LES solver with a fully unstructured grid. Far-field noise was predicted using an advanced-time formulation of the FW–H acoustic analogy.[9] They used both porous and impermeable (on the rod and airfoil surface) boundary approaches for evaluating the FW–H boundary integral and found little difference in the predicted noise. They also numerically investigated the effect of offsetting the airfoil in the cross-stream direction by the small amount observed in the experiments. That however did not significantly improve the agreement with the measured wake and velocity profiles. Jiang et al.[10] carried out a parametric study with different distances between the rod and the airfoil using high-order implicit LES. The far-field noise was predicted using the FW–H acoustic analogy.

This article presents an aeroacoustic analysis of the rod–airfoil problem using incompressible LES. Two different airfoil geometries are analyzed: one with a straight leading edge as in the experiments and the other with a serrated leading edge. Near-field hydrodynamics and far-field acoustic results are compared against measured data where available for the straight-edge case.

The pimpleFoam solver from OpenFOAM is used as the LES solver. Unsteady pressure on the airfoil surface is extracted from the simulations and used with Amiet's formula,[11] which extends Curle's theory to predict noise from distributed dipole sources over a thin airfoil. It should be emphasized that Curle's analogy is used in the most general sense and no approximations, e.g., thin-airfoil theory for computing lift and isotropic turbulence, typically associated with Amiet's theory are made here. A frequency-based correction given by Seo and Moon[12] is utilized to account for the difference in the airfoil span lengths between the simulation and the experiment. Curle's analogy to predict far-field noise for this rod–airfoil configuration has not been utilized before in available literature.

Previous experimental and numerical investigations[13–17] have shown substantial reduction in inflow turbulence (broadband) noise with the use of leading edge serrations. Almost all

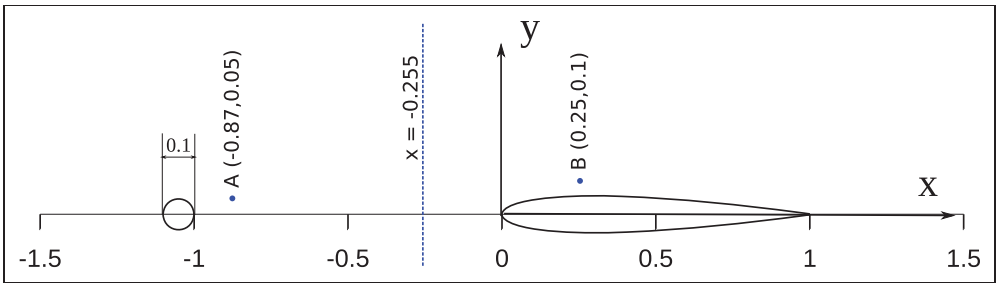

Figure 2. A 2D schematic showing the non-dimensional size, positions of the rod and the airfoil, and the near-field locations (points and lines in blue) where comparisons are made with experimental data.

these investigations have used homogeneous and grid-generated turbulence. In this article, we analyze the effectiveness of leading edge serrations in mitigating noise for the rod–airfoil configuration. The use of leading serrations for this configuration has not been numerically investigated before. The numerical approach to analyze the serrated case is the same as that used for the straight-edge case.

Numerical setup

Figure 2 shows a non-dimensional schematic of the rod–airfoil problem where length is non-dimensionalized by the airfoil chord. Also, velocity and density are non-dimensionalized by the speed of sound and the freestream density, respectively. The rod and the airfoil are placed in tandem along the x direction, the span direction is along the z axis, and the y direction is given by the right-hand rule.

In the experiments by Jacob et al.,[1] two different rod diameters were tested. In this article, we focus on the experiment with the rod diameter, $d = 0.1 \times c$, where c is the airfoil chord. Measurements were made for several Reynolds numbers and we limit our focus to $Re_d = 48\,\mathrm{K}$ (based on d) since at that Re, broadband noise contribution is apparent in the data. The distance between the rod trailing edge and the airfoil leading edge is equal to the airfoil chord c.

The airfoil is set at zero angle of attack in the simulations, as was intended in the experiments. However, based on the measured data, Jacob et al.[1] suspect that in the experiments, the airfoil might have been at a slight ($\sim 2^\circ$) angle of attack and slightly offset in the y direction. These geometric anomalies are not incorporated in the numerical model as a previous study[8] has shown that their effect on the far-field OASPL is less than 1 dB at 90°.

Computational mesh

Figure 3 shows a cross-sectional view of the mesh with the gridlines shown in the bottom half and only the block boundaries shown in the upper half. The far-field computational boundary (not shown) is nearly circular with a radius of approximately $11 \times c$. The geometry is essentially 2D and is extruded in the third, spanwise direction to obtain a 3D mesh. A reduced span length of $0.3 \times c$ is used in the simulations to reduce the mesh size and computation time. This choice is guided by previous works,[4–6] which also used partial span ($0.3 \times c$) domain in their simulations. "Frequency-Dependent Correction" section of this

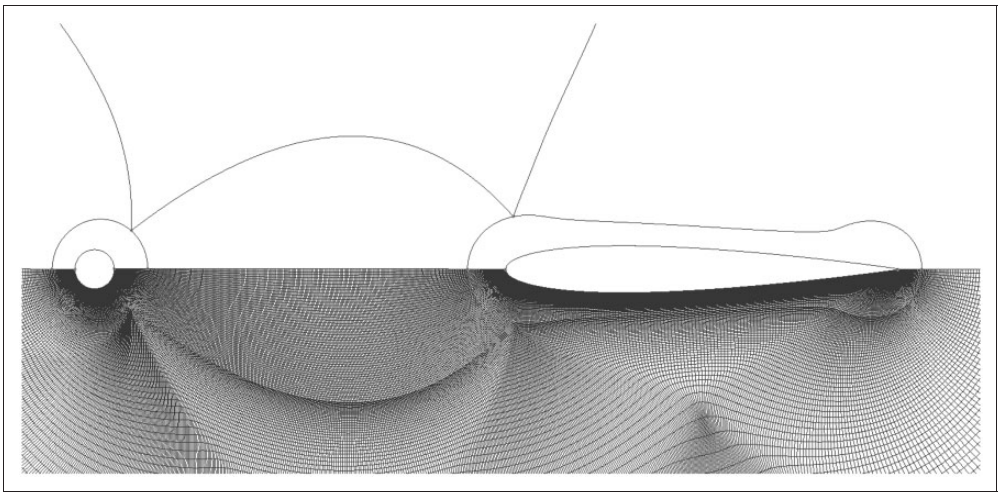

Figure 3. Cross-sectional (x–y) view of the near-field computational domain showing the block boundaries in the upper half and the grid lines in the lower half.

paper discusses the aeroacoustic implications of this choice. In order to compare with the measurements, the predicted noise spectra are scaled using the approach by Seo and Moon[12] to account for the difference in span lengths between the experiments and simulations.

A fully structured mesh generated using Pointwise (www.pointwise.com/pw) is used for the simulations. A planar mesh is first generated in the $z = 0$ plane, which is then repeated along the span with a uniform spacing to obtain the 3D mesh. The planar mesh is generated in three steps. The first step involves extruding the curves that define the rod and airfoil surfaces in the surface normal directions. This process yields high-quality orthogonal quadrilateral elements which are suitable for resolving wall boundary layers. The second step is to create quadrilateral elements between the rod and airfoil that are fine enough to capture the rod wake accurately. This is done by creating two parabolic curves, one each on the upper and lower sides, between the outer boundaries of the earlier extruded domains. These parabolic curves are then filled with quadrilateral elements with aspect ratio of nearly 1. The final step requires a closed curve encompassing the three domains: the rod and airfoil boundary layer regions and the rod wake region. In the final step, this closed curve is extruded normally until the outer radius is about $11 \times c$. This process gives a good quality mesh throughout the domain. Figure 3 shows a zoom view of the final 2D mesh in the $z = 0$ plane.

The blocking structure and the grid density are designed to resolve (a) the turbulence in the rod wake in the gap region, (b) the boundary layer on the rod, and (c) the boundary layer on the airfoil. The first cell height on the airfoil and the rod is chosen such that $y^+ = y/(\nu\sqrt{\rho/\tau_w}) = 1$, where ν is the fluid kinematic viscosity, τ_w is the wall shear stress, and ρ is the fluid density. This is a conservative estimate, since such small first cell height is required for resolving wall boundary layers. The problem under investigation is the interaction of the turbulence in the rod wake with the airfoil. Hence, accurate resolution of the turbulence generated in the airfoil boundary layers is not of paramount importance. This conservative approach was still taken however with the intent that in the future, the same

grid could be used to study "self" (trailing edge) noise from this airfoil and a comparison could be made between "self" noise and inflow (coming from rod wake) turbulence noise.

The total number of cells in the computational mesh is approximately 19 million. There are five boundary surfaces: rod, airfoil, two periodic and one far-field. Mesh quality metrics are as follows: the maximum cell aspect ratio is 169, the maximum mesh non-orthogonality is 30.5°, and the maximum skewness is 0.65.

Flow conditions and non-dimensionalization

The simulations are setup in non-dimensional variables denoted by the overhead tilde and the freestream values are used for non-dimensionalization. Therefore, the non-dimensional freestream density ($\tilde{\rho}_\infty$), speed of sound ($\tilde{a}_{0_\infty}$), and temperature ($\tilde{T}_\infty$) are all unity. Using $\tilde{\rho}_\infty = 1$ and $\tilde{a}_{0_\infty} = 1$, we get $\tilde{p}_\infty = 1/\gamma = 0.7143$. The freestream velocity is obtained as $\tilde{u}_\infty = 0.2$ from $\tilde{a}_{0_\infty} = 1$ and $M_\infty = 0.2$. The length scale is normalized w.r.t. the airfoil chord length, and hence, the diameter of the rod in the non-dimensional units is $\tilde{d} = d/c = 0.1$. The required Reynolds number of the flow based on the rod diameter, i.e., $Re_d = 48{,}000$ is obtained by setting the dynamic viscosity to $\tilde{\mu} = \tilde{\rho}_\infty \tilde{u}_\infty \tilde{d}/Re_d$ equal to 4.2×10^{-7}.

In physical units, the freestream conditions are $\rho_\infty = 1.226\,\mathrm{kg/m^3}$, $a_{0_\infty} = 360.0$ m/s (henceforth denoted by a_0), $u_\infty = 72$ m/s, and $p_\infty = 113{,}500$ Pa. The ratios of physical units to non-dimensional units are required for direct comparisons with measurements. The ratio of dimensional to non-dimensional time is $t/\tilde{t} = u_\infty/c = 720$ s, where $c = 0.1$ m. All spectral results are plotted w.r.t. Strouhal number based on the rod diameter, $St = fd/u_\infty$.

Incompressible flow solver, pimpleFoam

Equation (1) gives the filtered Navier–Stokes equation for incompressible LES computations,[18] where, $\widehat{(\,)}$ and $\tau_{ij}^{SGS} (= \widehat{u_i u_j} - \hat{u}_i \hat{u}_j)$ represent a homogeneous LES filter and subgrid stress, respectively. The governing equations are the continuity and momentum equations, written in differential form here as

$$\frac{\partial \hat{u}_i}{\partial x_i} = 0; \qquad \frac{\partial \hat{u}_i}{\partial t} + \frac{\partial \hat{u}_i \hat{u}_j}{\partial x_j} = -\frac{1}{\rho}\frac{\partial \hat{p}}{\partial x_i} + \nu \nabla^2 \hat{u}_i - \frac{\partial \tau_{ij}^{SGS}}{\partial x_j} \tag{1}$$

The subgrid stress (τ_{ij}^{SGS}) cannot be computed directly and requires modeling. Equation (2) gives the standard Smagorinsky[19] model which is an eddy viscosity type model to compute the subgrid stresses, where $S_{ij} (= (\partial \hat{u}_i/\partial x_j + \partial \hat{u}_j/\partial x_i)/2)$ is the rate-of-strain tensor that can be directly computed.

$$\tau_{ij}^{SGS} = -2(C_s \Delta)^2 \hat{S}_{ij} \sqrt{2 \hat{S}_{ij} \hat{S}_{ji}} \tag{2}$$

The transient, incompressible flow solver, pimpleFoam is used in LES mode with subgrid stresses computed using equation (2). The continuity and momentum equations (equation (1)) are solved using the PIMPLE algorithm, which is a combination of the pressure-implicit split-operator (PISO) algorithm[20] and the semi-implicit method for pressure linked equations (SIMPLE) algorithm.[21] The PIMPLE algorithm allows the Courant Friedrichs Lewy (CFL) number to be greater than unity while still maintaining numerical stability. A second-order implicit scheme is used for time marching and a time step of 0.005 is chosen.

The flowfield is initialized with the non-dimensional velocity, $\tilde{u}_\infty = 0.2$, gauge pressure set to zero, and kinematic viscosity specified as $\tilde{\nu} = 4.2 \times 10^{-7}$.

At the outer boundary, the velocity switches between zero gradient for outflow and fixed (prescribed) value for inflow. The boundary condition for pressure is zero gradient, which fixes the flux across the boundary using the freestream velocity. Gaussian integration with linear central differencing interpolation is used to compute gradients, Laplacian, and divergence terms. Divergence for the convective term is computed using linear upwind differencing interpolation.

Far-field noise prediction

Time-resolved pressure data on the airfoil surface is used with Curle's analogy to predict far-field noise. Curle's analogy can be used to predict noise radiation due to surface (dipole) sources. Due to the small flow Mach number in this problem, the noise sources are primarily the unsteady forces (dipoles) on the airfoil and the rod. Hence, the use of Curle's analogy to compute far-field sound is justified. The contribution to far-field noise from off-surface (quadrupole) sources has been shown to be significant only at very high ($St > 1$) and very low ($St < 0.05$) frequencies.[8] Giret et al.[8] showed that the quadrupole sources have little effect on the overall sound pressure level (OASPL). Eltaweel and Wang[6] also ignored the volume sources in their prediction methodology.

Far-field noise prediction

Pressure data are collected on the airfoil surfaces at a high sampling rate after the initial transients have been removed from the simulations. Using this surface pressure data, the unsteady lift per unit area (difference in pressures, $\Delta p(x, z, t)$ between the upper and the lower surfaces of the airfoil) is computed for all points (x, z) on the blade (airfoil) planform at each time, t. Note that x is along the chord and z is along the span. Amiet[11] used the idea that far-field acoustic response can be computed by assuming dipole sources in place of unsteady surface loads and gave the following expression for sound power spectral density (S_{pp}) for acoustic pressure at any given point (x', y', z') in the far-field

$$S_{pp}(x', y', z', \omega) = \left(\frac{\omega y'}{4\pi a_0 \sigma^2}\right)^2 \iiiint S_{qq}(x_1, x_2, z_1, z_2, \omega) \times e^{\frac{i\omega}{a_0}\left[\beta^{-2}(x_1 - x_2)(M_\infty - x'/\sigma) + z'\eta/\sigma\right]} \, \mathrm{d}x_1 \, \mathrm{d}x_2 \, \mathrm{d}z_1 \, \mathrm{d}z_2 \tag{3}$$

where $\beta = \sqrt{1 - M_\infty^2}$, $\sigma = \sqrt{x^2 + \beta^2(y^2 + z^2)}$, η is the spanwise separation, and S_{qq} is the cross power spectral density (PSD) of predicted unsteady pressure difference (Δp) between any two points (x_1, z_1) and (x_2, z_2) on the planform. S_{qq} is computed using Welch's average periodogram method[22] for all point pairs and is then used with equation (3) to numerically compute the far-field S_{pp}. Theoretical background on the spectral analysis used here is provided in Appendix 1.

Kato's correction

The span length of the rod–airfoil assembly simulated in the present calculations is smaller than the experimental model. The predicted far-field noise therefore has to be corrected before comparing with the measured data. The correction that needs to be applied to the

predicted spectra depends on spanwise coherence. If we denote spanwise coherence length by L_c and use subscripts s and e for the simulations and the experiment respectively, then equation (4) can be used for comparing the measured and the predicted spectra.

$$\begin{aligned}
\left(S_{pp}(\omega)\right)_e &= \left(S_{pp}(\omega)\right)_s + 20\log(L_e/L_s) \;\forall\; L_s < L_e < L_c, \\
\left(S_{pp}(\omega)\right)_e &= \left(S_{pp}(\omega)\right)_s + 10\log(L_e/L_s), \;\forall\; L_c < L_s < L_e, \\
\left(S_{pp}(\omega)\right)_e &= \left(S_{pp}(\omega)\right)_s + 20\log(L_c/L_s) + 10\log(L_e/L_c) \;\forall\; L_s < L_c < L_e
\end{aligned} \tag{4}$$

Equation (4) assumes that there is perfect correlation over the span length of L_c, outside of which, the correlation drops identically to zero. This 'box-car' simplification by Kato and Ikegawa[23] is often used. The span length of the rod and airfoil assembly in the simulations (L_s) is three times the rod diameter (d), i.e., $L_s = 3d$, which is one-tenth of the span length of the model used in the experiment, i.e., $L_e = 10L_s$. Assuming that the correlation length L_c is less than L_s, the correction required is

$$\begin{aligned}
\left(S_{pp}(\omega)\right)_{s\,corr} &= \left(S_{pp}(\omega)\right)_s + 10\log(L_e/L_s), \text{ or,} \\
\left(S_{pp}(\omega)\right)_{s\,corr} &= \left(S_{pp}(\omega)\right)_s + 10\log(10)
\end{aligned} \tag{5}$$

The spanwise correlation length in this problem is a strong function of frequency: the correlation length is very large at the peak shedding frequency and its harmonics but small at other frequencies. This highlights the need for a frequency-dependent span-correction for noise prediction. This issue and a potential resolution are discussed in "Frequency-Dependent Correction" section.

Results and data comparisons

The phenomena of interest in the problem under investigation are unsteady but statistically stationary. The interest is not in transient phenomena such as instantaneous/impulsive start of the rod/airfoil combination. In the experiments, the wind tunnel was started and the rig allowed to reach a statistically stationary state before measurements were taken. Similarly, the computations have to reach a statistically stationary state before any unsteady data can be gathered from the simulations. Removal of initial transients from the computational domain is therefore required before meaningful results can be sampled. The time period of wake shedding from the cylinder for $Re_d = 48{,}000$ is approximately 2.6 non-dimensional time units. The data collection began after 40 time units and then sampled for approximately 40 shedding periods (approximately 104 time units) in the simulation. These data are used for the statistical analysis presented in the following sections.

Mesh sensitivity study

A mesh sensitivity study is carried out with three mesh sizes comprising of 10-, 19-, and 64-million cells. The different meshes are generated by refining the grid in the wall-normal and streamwise directions while maintaining the spanwise grid count at 80. The first cell height is maintained to give a y^+ of unity when refining in the wall-normal direction.

Figure 4 plots the results of the mesh sensitivity study. The PSD of the x-component of velocity ($S_{uu}(\omega)$) at point A ($-0.87c, 0.05c$) is shown in subplot (a). Subplots (b) and (c), respectively, show the predicted mean ($\bar{C}_P$) and root mean square (rms) ($C_{P,rms}$) of the coefficient of pressure on the rod surface. All these quantities are averaged along the span

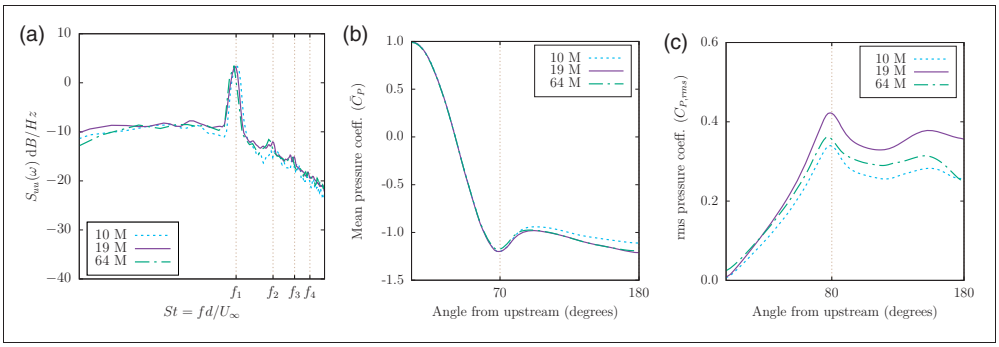

Figure 4. Results of the mesh sensitivity study: (a) PSD of the *x*-component of velocity at point A, and time- and span-averaged (b) C_P- and (c) $C_{P,rms}$ distributions on the cylinder surface.
rms: root mean square.

in the plots. Grid convergence is observed beyond the 19-M mesh in the hydrodynamic spectra in the cylinder wake as well as in the mean surface pressure on the cylinder surface (see Figure 4(a) and (b)). There is, however, a perceptible dependence on mesh in predicting the rms of aerodynamic pressure on the cylinder surface (Figure 4(c)). Since the noise source of interest here is due to the cylinder wake interacting with the airfoil, and the fact that no statistically significant change is observed in the cylinder wake velocity spectra by increasing the mesh beyond 19 M cells, the 19-M mesh is deemed sufficient to study aerodynamic noise for this problem and to investigate aeroacoustics effects of serrations on the airfoil. Furthermore, the wall-clock times for simulating a unit non-dimensional flow time using 128 processors for the 10 M, 19 M, and 64 M cell meshes are 759, 2315, and 34,569 s, respectively. The wall-clock time increases by a factor of 15 as the mesh size increases from 19 M to 64 M. This large increase coupled with limited parallel scalability of the flow solver (OpenFOAM does not scale beyond 512 processors) make it intractable to attempt a larger mesh size.

Based on the mesh sensitivity study, the 19-M mesh simulation results are used for experimental validation described in the following section.

Experimental validation

Rod surface pressure statistics. Pressure distributions on the rod and airfoil surfaces are obtained by averaging the time-accurate data (sampled over 40 shedding periods) in time as well as in space (along the span direction). The mean pressure coefficient, $\bar{C}_P$, and the root mean squared pressure coefficient, $C_{P,rms}$, for the rod are obtained using this averaging procedure and compared against measurements in Figure 5 for the rod. The pressure coefficients are plotted w.r.t. angle measured from upstream. Thus, 0° and 180° denote the rod leading and trailing stagnation points, respectively.

Figure 5(a) shows that the expected value of 1 is obtained for $\bar{C}_P$ at the rod leading stagnation point after which $\bar{C}_P$ drops steadily until the peak negative value is reached at 70°. The peak location predicted by OpenFOAM matches with the experimental data from Norberg.[24] Two sets of data from Norberg[24] are shown, which correspond to Re_d of 20,000 and 60,000. The agreement between the predictions and the measured data is very good.

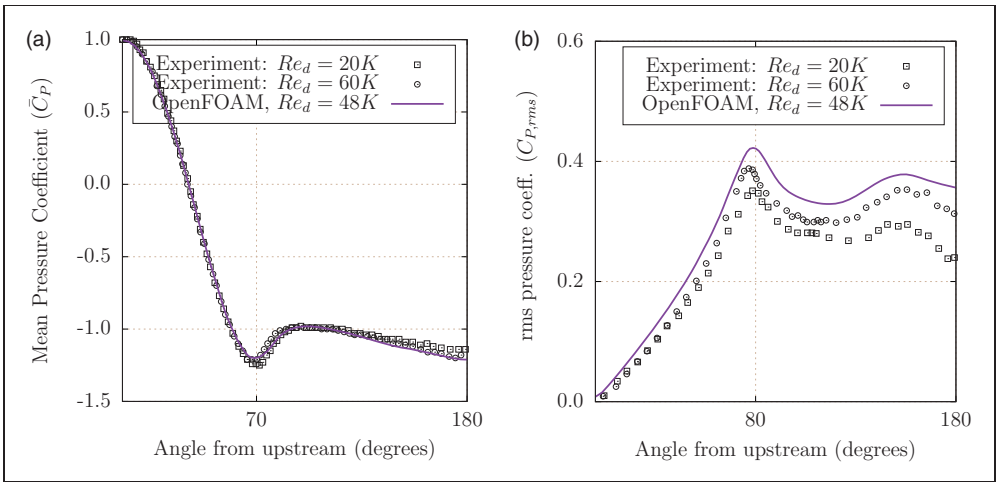

Figure 5. Mean and rms aerodynamic pressure coefficients on the rod. Experimental data in these plots is from Norberg.[24] rms: root mean square. (a) Mean pressure coeff., $\bar{C}_P$. (b) RMS pressure coeff., $C_{P,rms}$.

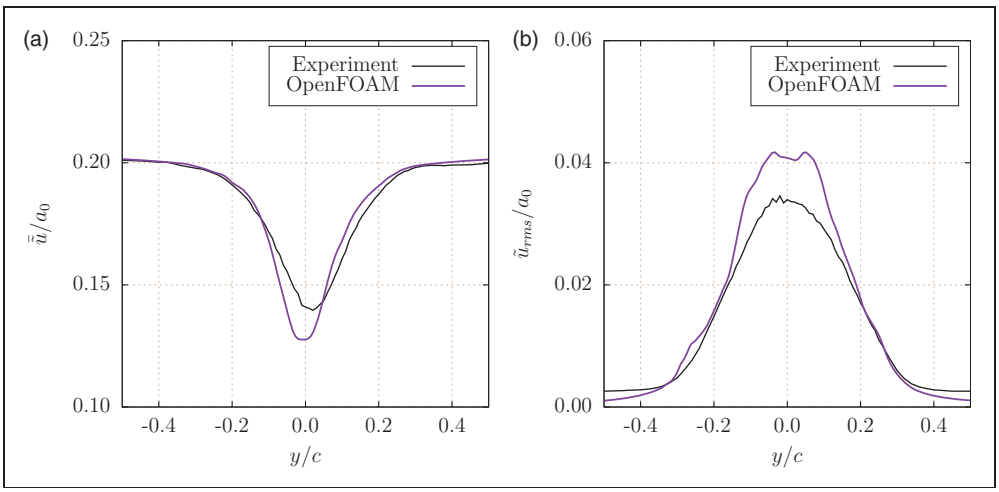

Figure 6. Profiles of mean and rms of the *x* component of velocity in the rod wake at station $x = -0.255$ c. (a) u mean, (b) u rms.

Figure 5(b) shows that $C_{P,rms}$ starts from zero at the rod leading edge and then monotonically increases with angle from upstream until 80°, after which it drops rapidly. The flow separates approximately between 75° and 80° as observed by Achenbach.[25]

X-velocity statistics in rod wake. Figure 6 compares profiles of the mean and the rms of the x-component of velocity in the rod wake at $x = -0.255\,c$. The momentum deficit and turbulence intensity in the wake are slightly over predicted. The measured profiles show a shift

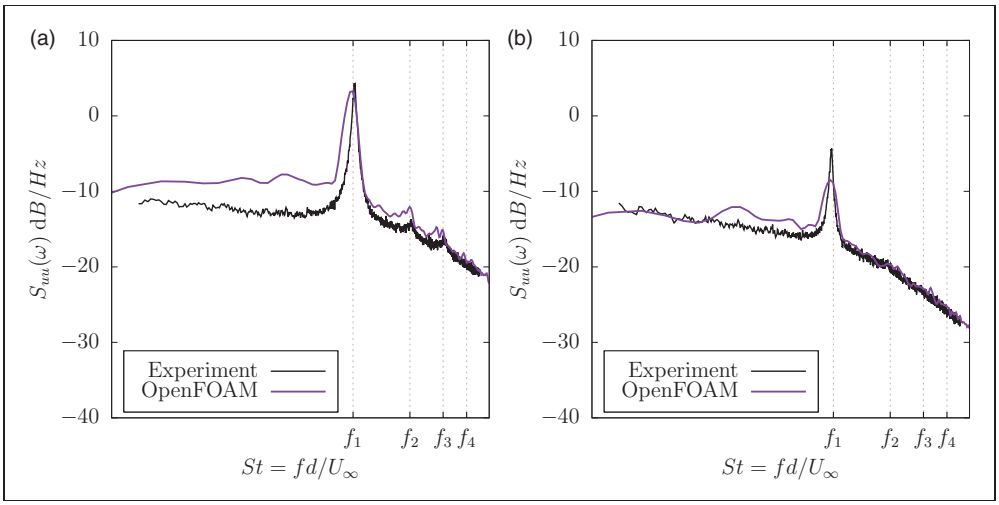

Figure 7. Velocity power spectral density, $S_{uu}(\omega)$ dB/Hz, plotted against Strouhal number at points "A" and "B" from Figure 2. (a) Spectra at point "A", (b) Spectra at point "B".

in the y direction, which is due to the slight offset in the experiment as noted in Jacob et al.[1] The predicted profiles are symmetric about the $y = 0$ plane since this offset is not modeled in the simulations.

X-velocity spectral comparisons. Measurements of near-field PSD of velocity are available at a few locations close to the rod and the airfoil. PSD and other related quantities are defined in Appendix 1. The predicted near-field velocity spectra are compared against the measured data at two locations. These are marked as "A" and "B" in Figure 2. Instantaneous velocity data were gathered from the simulations at the two locations for 135 periods of wake shedding. The spectra were computed at all spanwise locations and averaged. Figure 7 shows the axial velocity PSD comparisons at points "A" and "B." Two essential features of the measured spectra, (1) the spectral peak amplitude at $St \sim 0.19$ and (2) the decay beyond the spectral peak, are captured well by the predictions. The second and third harmonics are also captured in the simulations. In Figure 7 and all subsequent spectra plots, this wake shedding frequency ($St \sim 0.19$) is denoted by f_1 and its second, third, and fourth harmonics by f_2, f_3, and f_4, respectively. The Strouhal numbers corresponding to f_1, f_2, f_3, and f_4 are 0.19, 0.38, 0.57, and 0.76, respectively.

The magnitude of the spectral peak improves for 64 million meshes. However, the magnitude of the spectral peak for far-field noise does not improve with 64 million meshes. This along with the unrealistic estimate for computational time for a similar fine mesh for serrated leading edge geometry discourages the usage of such a fine mesh for the present study.

Far-field spectra. Figure 8 compares the predicted far-field acoustic pressure PSD against the data measured at a point directly above the airfoil leading edge at a distance of $18.5\,c$. The predictions are made using Curle's analogy with the pimpleFoam simulation data and the default span-length correction given in equation (5) is used. The predicted spectrum

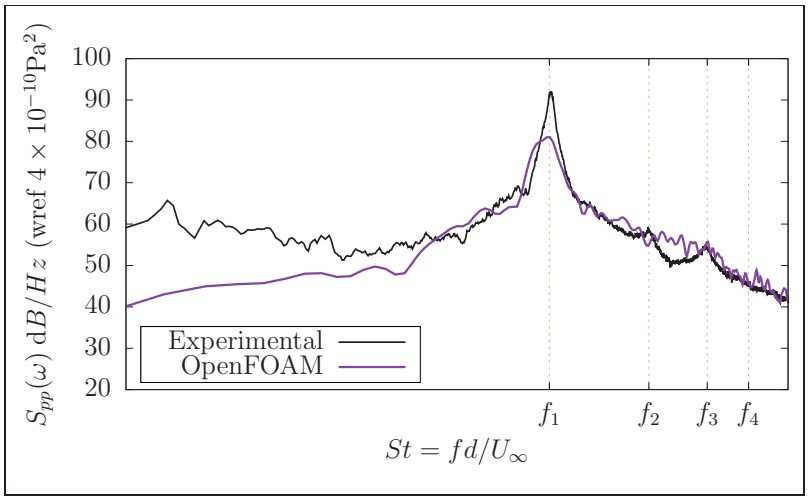

Figure 8. Far-field pressure spectral density (PSD) directly above the airfoil leading edge ($\theta = 90^\circ$) at a distance of 18.5 chords. Prediction using the Curle's analogy and constant Kato's correction (equation (5)) is compared with measured data.

in Figure 8 is obtained by spectral averaging over multiple time segments to reduce statistical scatter. The spectral peak frequency (f_1) and the spectral fall-off for $f > f_1$ are reasonably well captured by the simulations; however, the peak amplitude is underpredicted. "Frequency-Dependent Correction" section discusses this issue in detail and describes a method to improve the prediction accuracy.

Spectral properties of unsteady lift

Figure 9 shows contours of PSD of the unsteady pressure difference across the airfoil surface. The abscissa and the ordinate denote the location along the chordwise direction and Strouhal number, respectively. Figure 9(a) shows that the highest unsteady pressure difference is concentrated towards the leading edge for $0 < St < 0.5$, and near the peak shedding frequency ($St \sim f_1$), a large region of the airfoil (up to $x/c \sim 0.7$) also shows high levels of unsteady pressure difference. Figure 9(b) is plotted with the abscissa on a log scale to highlight the PSD distribution near the leading edge. The maximum value of the PSD is found at $x/c = 0.00647$. This illustrates the maximum noise source strength location. This chordwise location is used as a representative source position to study spanwise coherence later in "Far-field Sound Spectra" section.

Frequency-dependent correction

The correction suggested by Kato and Ikegawa[23] to account for differences in span lengths between experiments and simulations was enhanced by Seo and Moon[12] by recognizing the dependence of spanwise coherence on frequency. Figure 10(a) plots spanwise coherence (γ^2) of the predicted unsteady pressure difference (Δp) across the airfoil surface at the quarter-chord point ($x/c = 0.25$). It is evident that spanwise coherence is a strong function of

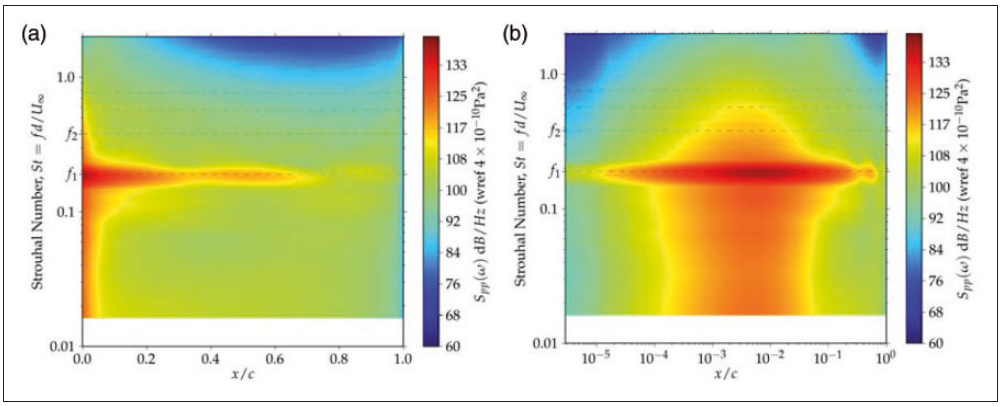

Figure 9. Power spectral density for pointwise force on the airfoil, ΔP. (a) Linear scale for x/c, (b) Log scale for x/c.

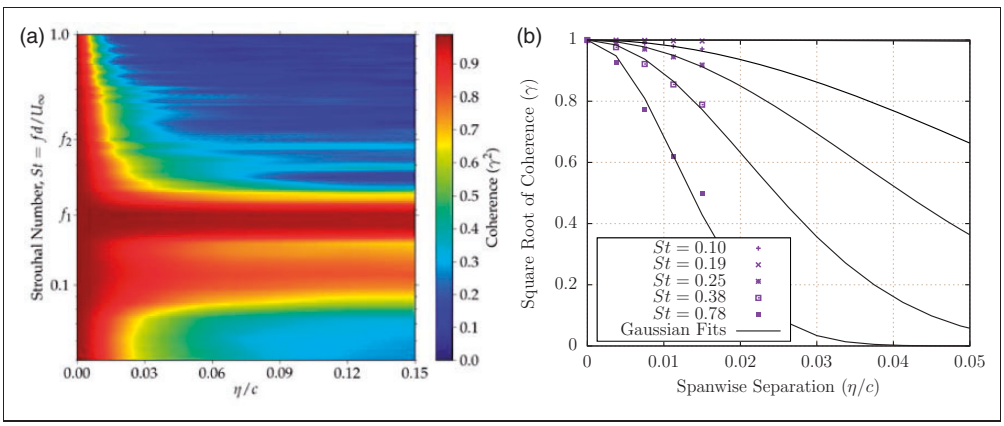

Figure 10. Coherence data from the simulations and the computed spanwise coherence lengths. (a) Coherence data, (b) spanwise coherence lengths.

Strouhal number (frequency) for this problem. Very high correlation is observed near the peak frequency f_1, but it steeply drops off at other frequencies.

The formula to correct the predicted sound pressure level for mismatched span lengths given by Seo and Moon[12] is

$$SPL_c(\omega) = 10\log\left[\sum_{i=1}^{N}\sum_{j=1}^{N}\exp\left(-(i-j)^2\left(\frac{L_s}{L_c(\omega)}\right)^2\right)\right] \tag{6}$$

where L_s, $L_c(\omega)$, and N, respectively, are the simulated model span length, the frequency-dependent spanwise coherence length, and the number of simulated lengths required to match the long-span used in experiments (L_e), i.e., $N = L_e/L_s$. Figure 11 shows a schematic comparing the two span lengths where N-sections of simulated length (L_s) are repeated to match the experimental length (L_e).

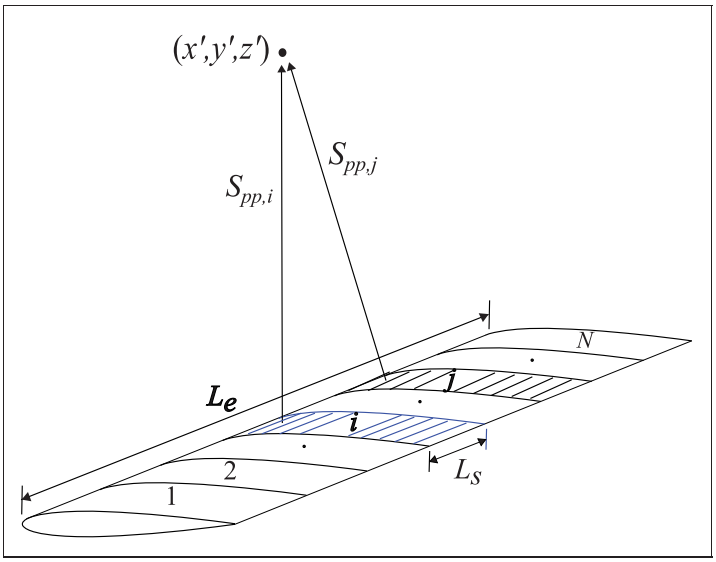

Figure 11. A schematic comparing the simulated- (L_S) and the experimental (L_E) span lengths.

In the present simulations, $L_s = 0.3c$, $L_e = 3c$ and thus $N = 10$. Square root of the spanwise coherence is assumed to follow a Gaussian distribution with separation distance (Δz) as in equation (7). The method of least squares is used to fit the predicted coherence ($\gamma^2(\eta, St)$) data, shown in Figure 10(a), with equation (7) to obtain $L_c(\omega)$ for each frequency. Gaussian fits are shown along with the data for a few frequencies in Figure 10(b).

$$\gamma(\Delta z) = \exp\left(-\frac{\Delta z^2}{L_c(\omega)^2}\right) \tag{7}$$

Using equation (6) with the spanwise coherence lengths computed to fit Gaussian distribution at each frequency gives the required correction in the predicted sound pressure spectral density, S_{pp}. The correction in spectral density (dB/Hz) as calculated using equation (6) is shown in Figure 12(a). The measured far-field noise spectra are compared with the predictions made this new correction as well as that computed using the constant correction of equation (5) in Figure 12(b). The prediction for peak amplitude is substantially improved using the frequency-dependent span-length correction.

Noise mitigation using serrations

Serrations have been shown to be effective in reducing blade aerodynamic noise.[13–17] Blades with serrated trailing and leading edges have been used to mitigate corresponding edge noise sources. The focus of past numerical investigations on leading edge (inflow turbulence) noise mitigation has been on homogeneous, grid-generated turbulence. Here, we investigate one serration geometry to mitigate aerodynamic noise for the rod–airfoil configuration. The baseline NACA 0012 airfoil is replaced with a corresponding airfoil with leading edge serrations. The leading edge of the serrated airfoil is defined in equation (8) as a sinusoid of wavelength, $\lambda = 0.3\ c$ and amplitude of $0.06\,c$. The simulated span length is kept the same

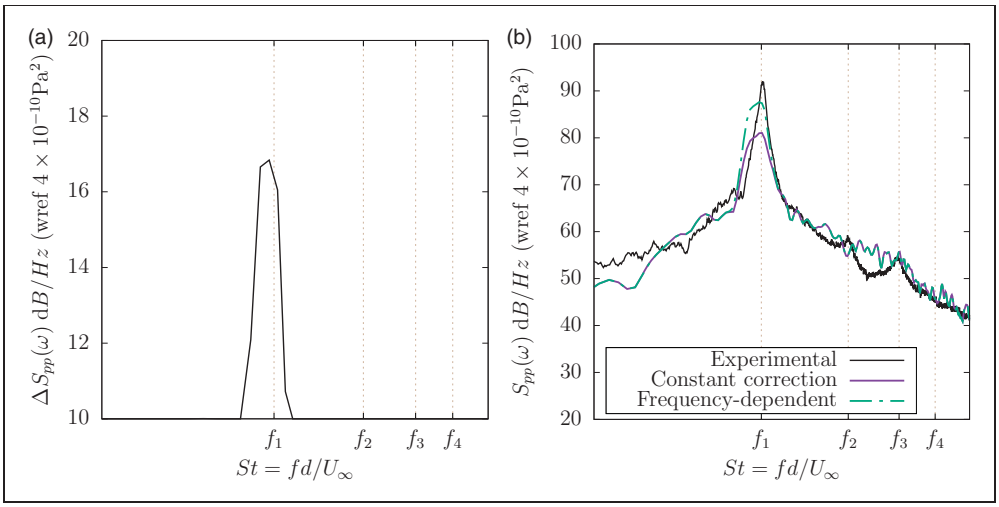

Figure 12. Comparison of measured far-field noise against predictions with span corrections: (a) coherence-based correction as computed using equation (6), and (b) span-corrected spectra compared against measurements. In (b), "Constant correction" refers to Kato's correction (equation (5)) and "Frequency-dependent" refers to the coherence-based correction given by equation (6).

(=0.3 c) as for the baseline geometry, which accommodates one wave of the serrations in the simulated domain; periodic boundary conditions are employed in the span direction as for the baseline geometry.

$$x_{LE}(z) = -0.06c\cos(2\pi z/(0.3c)), 0 < z < 0.3c \tag{8}$$

Figure 13 shows the serrated blade geometry. It has the longest chord (serration peak) at the two spanwise ends, the shortest chord (valley) in the middle, and the mean chord is kept equal to the baseline airfoil chord to maintain aerodynamic similarity between the two geometries. The surface is generated by scaling the "front" portion of the airfoil at each spanwise location by the corresponding chord length. The "front" portion is defined as the region between the leading edge and the maximum thickness location ($0 \le x \le 0.3c$). Restricting the modifications to this region ensures that the serrations directly affect the flow only in the favorable pressure gradient region of the airfoil. Equation (9) is the thickness distribution of the serrated wing geometry, where the function, $f(x)$ specifies the thickness of the baseline NACA 0012 airfoil for $0 \le x \le c$. Equations (8) and (9) together completely define the serrated airfoil geometry.

$$y(x,z) = \begin{cases} f\left(0.3c\ \frac{x - x_{LE}(z)}{0.3c - x_{LE}(z)}\right), & x_{LE}(z) \le x < 0.3c \\ f(x), & 0.3c \le x \le c \end{cases} \tag{9}$$

The meshing strategy for the serrated geometry is different from the baseline geometry as it is highly 3D. Keeping the same boundary layer block for the rod, a 3D hyperbolic normal extrusion is performed starting from the surface of the serrated wing to the constructed boundary layer block around the wing. As in the baseline case, parabolic curves are created

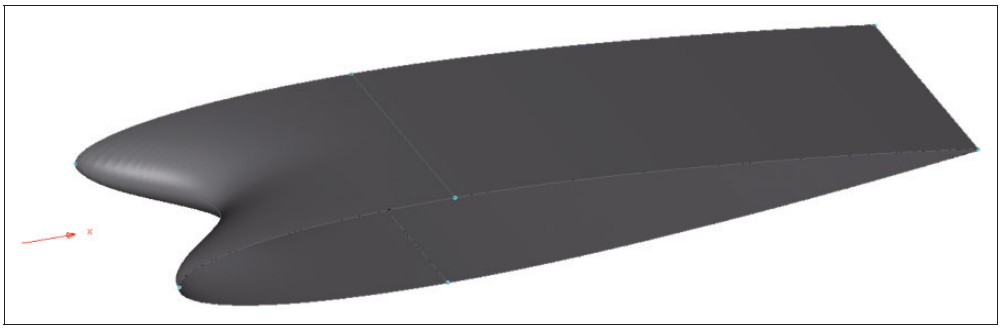

Figure 13. Schematic showing the serrations on the leading edge.

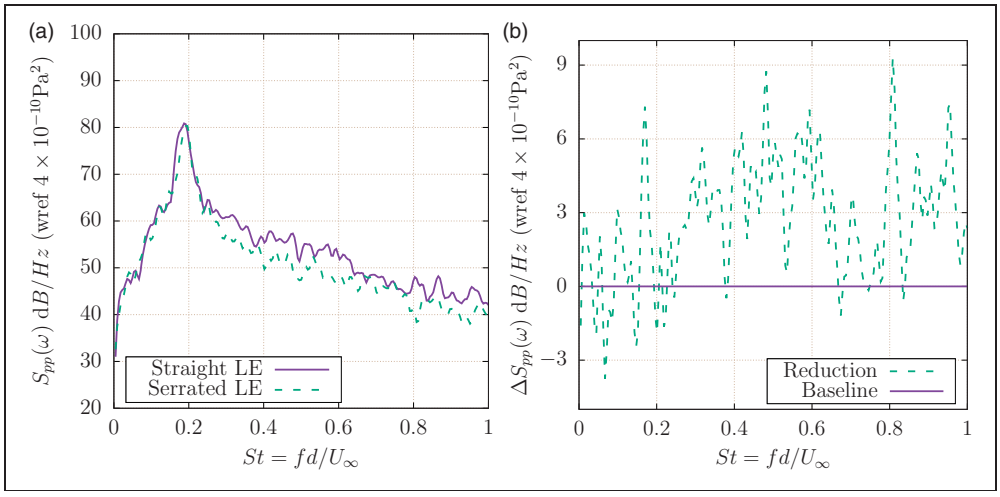

Figure 14. Far-field noise comparison at (0, 18.5 *c*). (a) Noise Spectra, (b) Reduction in noise.

between the rod and the wing boundary layer blocks and cells are created between the two boundary layer blocks. For the last step, the outermost surfaces of these blocks are collectively extruded normally to the far-field, which is nearly circular with a radius of 11 c. The mesh has roughly 19 million cells, which was found to be sufficient in the mesh sensitivity study (see ''Mesh Sensitivity Study'' section). However, because of higher three dimensionality, this mesh has poorer orthogonality for the hexahedra cells in comparison to the mesh for the baseline geometry. This problem is addressed by employing additional pressure correction loops in the flow solver.

Far-field sound spectra

Figure 14 compares the predicted far-field sound pressure spectral densities for the baseline and the serrated leading edge geometries. A clear reduction in radiated broadband noise is observed at mid to high frequencies with the leading edge serrations; however, the peak

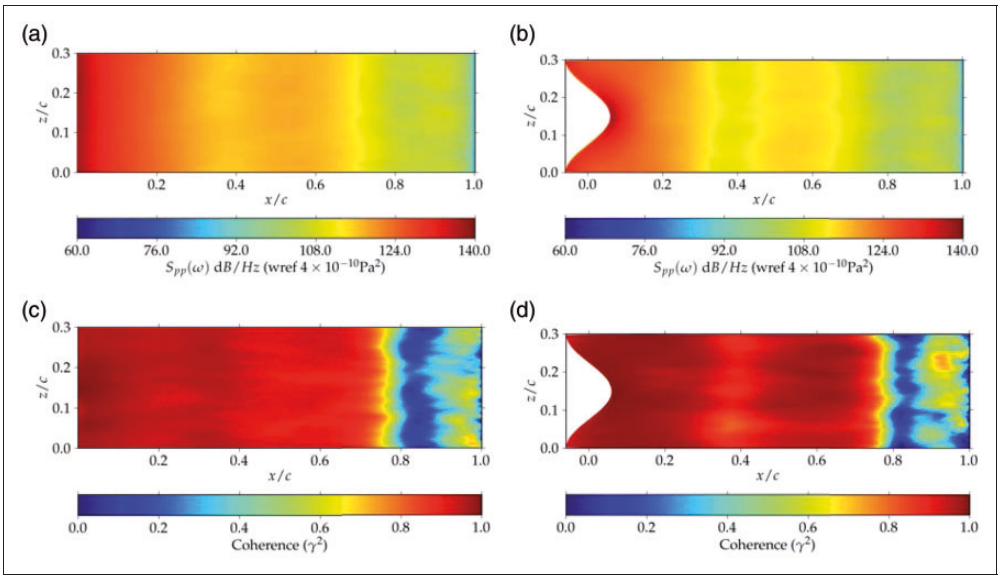

Figure 15. Comparison of noise sources between the baseline and serrated airfoils at the peak shedding frequency, $St = 0.19$: (a) Contours of power spectral densities of ΔP (S_{pp}) for the baseline, and (b) contours of S_{pp} for the serrated airfoil, (c) coherence (γ^2) for the baseline w.r.t. reference point (0.00647 c, 0.148 c), and (d) γ^2 for the serrated airfoil w.r.t. reference point at (0.06543 c, 0.147 c).

radiated sound pressure around $St \approx 0.19$ remains unchanged. The reduction in noise, measured as difference in power spectral densities ($\Delta S_{pp} = S_{pp}\text{baseline} - S_{pp}\text{serrated}$), is plotted separately in Figure 14(b). Integrating over the frequency gives an OASPL reduction of about 1.5 dB with the serrated leading edge geometry.

We investigate the airfoil unsteady surface pressures to diagnose the physical mechanisms behind noise reduction. Figure 15 compares the noise sources (PSD of difference in pressure between the pressure and suction sides of the airfoil, ΔP) at the peak frequency, $St = 0.19$ between the baseline and the serrated leading edge geometries. Figure 15(a) and (b) compares the magnitudes of the power spectral densities on the blade planform. While the peak magnitudes are located close to the leading edge, a substantial portion of the blade contributes to the radiated noise in both geometries. For the serrated blade geometry, there is a spanwise variation in S_{pp} magnitude near the leading edge—it is maximum around the peaks and the valley and minimum in-between.

Figure 15(c) and (d) compares the coherence, γ^2 (normalized magnitude of two-point spatial correlation) between the two airfoil geometries at the peak frequency. The reference points used to evaluate coherence are selected to be the points where the S_{pp} is maximum and these are found to be ($0.00647\,c$, $0.148\,c$) and ($0.06543\,c$, $0.147\,c$) for the baseline and the serrated airfoil geometry, respectively. The plots show that there is a very strong spanwise correlation at this frequency, as discussed previously in ''Frequency-Dependent Correction'' section. Also, the correlation along the chord is also very high, suggesting that the entire airfoil is radiating in unison. The wavelength of the sound radiated at $St = 0.19$ is $5.56\,c$, which is large compared to the source length scale, suggesting that the noise source could be

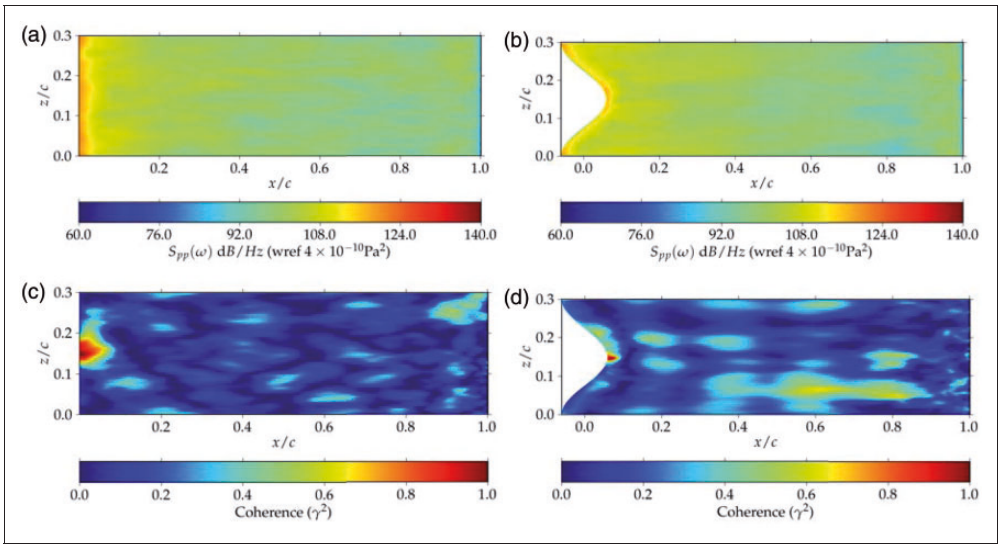

Figure 16. Contours of power spectral density of ΔP on blade planforms and coherence with respect to corresponding reference point at $St = 0.35$. (a) S_{pp} for straight leading edge, (b) S_{pp} for serrated leading edge, (c) γ^2 w.r.t. (0.00647 c, 0.148 c), (d) γ^2 w.r.t. (0.06543 c, 0.147 c).

treated as compact for the peak frequency radiation. One could therefore compute the integrated unsteady lift on the airfoil and use it as a point dipole source to approximate the peak noise radiation.

Figure 16 draws a similar comparison at a higher frequency ($St = 0.35$), which shows distinctively different features compared to the plots at $St = 0.19$. For both geometries, the PSD of unsteady pressure difference is highly concentrated near the leading edge and much reduced, compared to the values at $St = 0.19$. The spanwise variation is similar to $St = 0.19$—maximum S_{pp} near the peaks and the valley and minimum in-between. Figure 16(c) and (d) compares the coherence between the two geometries using the same reference points as before. The coherence is seen to be high only for a small region around the reference point. The chordwise distribution suggests the noise source is localized near the leading edge (for frequencies away from $St = 0.19$). It is further observed that the spatial region of high coherence reduces from the straight-edge case to the serrated-edge case. This spatial decorrelation contributes to the observed reduction in radiated far-field noise. These figures suggest that the reduction in far-field noise for the serrated case is caused both by the reduction in the unsteady pointwise lift and the reduction in the coherence region on the airfoil.

The region near the blade leading edge is examined in detail. Cross-spectral densities of Δp are evaluated on a curve along the blade span which is at a fixed distance from the blade leading edge. For straight leading edge case, this is a straight line with a distance of 0.00647 c from the leading edge. For the serrated leading edge case, it is a cosine curve with the same distance from the serrated (curved) leading edge. The distance of 0.00647 c is selected based on the finding in "Spectral Properties of Unsteady Lift" section that the maximum magnitude of Δp PSD on the airfoil planform occurs at that chordwise location.

Figure 17(a) and (b) contrasts the cross-spectral PSD drawn along the corresponding spanwise curves between the straight-edge and serrated-edge cases. The reference points to

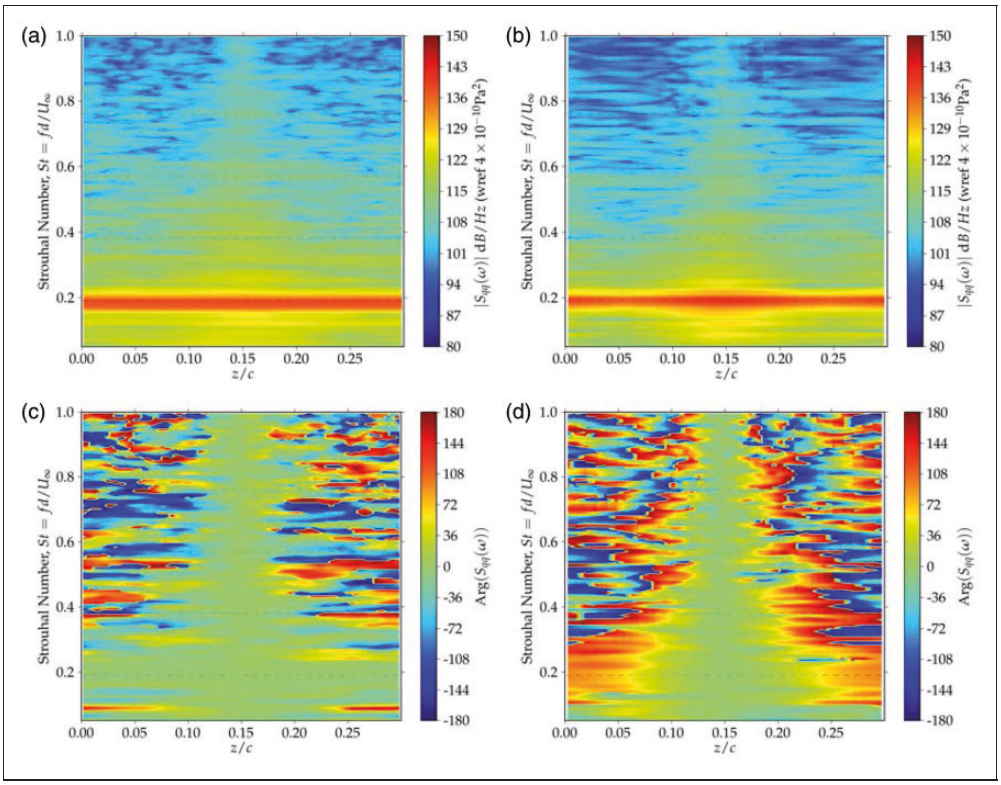

Figure 17. Contours of cross-spectral density magnitude and phase w.r.t. corresponding reference points along the leading edge curves. (a) $|S_{qq}(\omega)|$ for straight leading edge, (b) $|S_{qq}(\omega)|$ for serrated leading edge, (c) Arg($S_{qq}(\omega)$) for straight leading edge, (d) Arg($S_{qq}(\omega)$) for serrated leading edge.

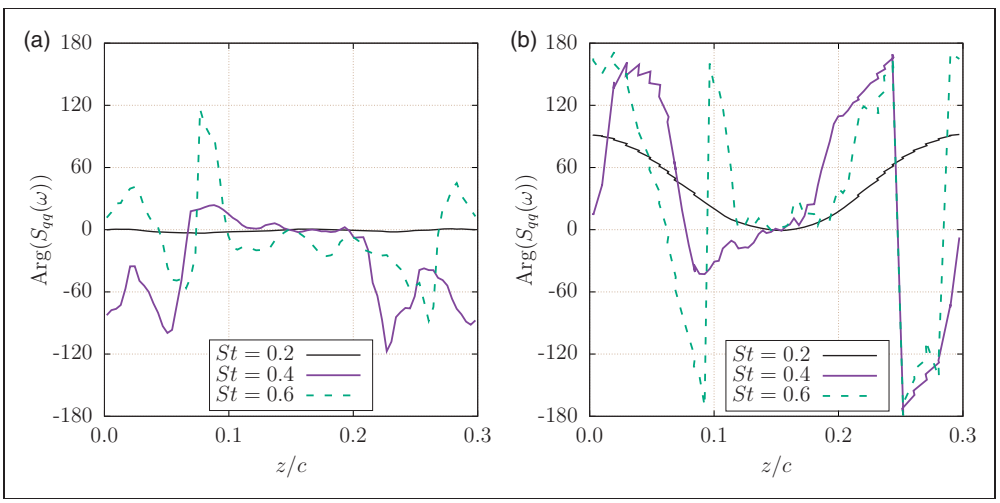

Figure 18. Predicted spanwise phase variation of cross-spectral density for a selected few frequencies. (a) Arg($S_{qq}(\omega)$) for straight leading edge, (b) Arg($S_{qq}(\omega)$) for serrated leading edge.

compute the PSDs are the same as used in Figure 16. A decrease in magnitude is observed for the serrated case over straight leading edge case between $St = 0.4$ and $St = 0.8$, which corresponds to a reduction in the noise source strength.

Figure 17(c) and (d) shows the phase of the cross-spectra. Higher spanwise phase variation is observed for the serrated-edge case at almost all frequencies. This is further demonstrated in Figure 18(a) and (b) by plotting the spanwise phase variation for a few selected frequencies. Higher spanwise phase variation for the serrated leading edge case is apparent in the plots. High phase variation reduces positive correlation over the coherent source region and, hence, leads to noise reduction via destructive interference at the observer. The concept of phase variation is utilized in the design of outlet guide vanes (OGVs) of turbomachines, which are swept backwards and lent in the circumferential direction, to reduce tonal noise from fan wake–OGV interaction.[26]

In summary, the leading edge serrations are found to (1) reduce the unsteady pressure magnitude near the leading edge, (2) reduce the spatial coherence of the source region, and (3) increase spanwise phase variation. Each of these mechanisms contributes to the observed noise reduction. Quantification of relative contributions to the observed noise reduction by these mechanisms will be investigated in a future study.

Conclusions

Incompressible LES are used to analyze aerodynamic interaction between a rod and an airfoil in a tandem arrangement. The noise produced due to this interaction is analyzed using Curle's acoustic analogy. The incompressible solver, pimpleFoam, coupled with Curle's analogy is benchmarked for noise prediction, validated against the rod–airfoil case, and used to analyze noise mitigation through leading edge serrations. A mesh sensitivity study was conducted and a 19-million cell mesh was found to be sufficient for this noise prediction methodology. The predicted mean and rms velocity profiles and surface pressure, near-field velocity spectra, and far-field acoustic pressure spectra are compared with measurements.

The predictions of mean surface pressure on the rod surface are in good agreement with the experiments, with the rms pressure overpredicted by about 9%. Mean flow comparisons show moderate agreement where velocity deficit and turbulence intensity in the wake are slightly overpredicted. The predictions of velocity PSDs in the near-field match well with the data in terms of capturing the peak frequencies and the spectral fall-off. Far-field PSD comparisons with data are made by using Kato correction to account for the differences in the span lengths. Good agreement with the data is observed except for peak amplitude at the vortex shedding frequency ($f_1 \sim 0.19$). The prediction of peak amplitude improves substantially by using the frequency-dependent correction methodology by Seo and Moon[12] with the coherence data from the simulation.

The noise prediction methodology is applied to a modified rod–airfoil problem where the leading edge of the airfoil is serrated; the serrations defined as a sinusoid. The serrations are found to be effective in the mid- to high-frequency range and provide a reduction of about 1.5 dB in the far-field OASPL. Analyses of surface noise sources suggest that following mechanisms contribute towards the observed far-field noise reduction: (a) the reduction in unsteady ΔP magnitude, (b) the reduction in spatial coherence over the source region, and (c) the increase in spanwise phase variation. Investigations to quantify the relative

contributions of these different noise reduction mechanisms will be undertaken as part of a future study.

Declaration of conflicting interests

The author(s) declared no potential conflicts of interest with respect to the research, authorship, and/or publication of this article.

Funding

The author(s) disclosed receipt of the following financial support for the research, authorship, and/or publication of this article: This research was funded by the National Science Foundation under grant number NSF/CBET-1554196 and the Iowa Space Grants Consortium (Grant #475-20-5). Computational resources used for this research were provided by NSF XSEDE (Grant # TG-CTS130004) and by the Argonne Leadership Computing Facility (ALCF) through an ALCC grant.

References

1. Jacob MC, Boudet J, Casalino D, et al. A rod-airfoil experiment as a benchmark for broadband noise modeling. *Theor Comp Fluid Dyn* 2005; 19: 171–196.
2. Agrawal BR and Sharma A. Numerical investigations of bio-inspired blade designs to reduce broadband noise in aircraft engines and wind turbines. In: *54th AIAA aerospace sciences meeting*, San Diego, CA, 2016, p. 0760. Reston, VA: AIAA.
3. Casalino D, Jacob M and Roger M. Prediction of rod-airfoil interaction noise using the Ffowcs-Williams-Hawkings analogy. *AIAA J* 2003; 41: 182–191.
4. Boudet J, Grosjean N and Jacob MC. Wake-airfoil interaction as broadband noise source: a large-eddy simulation study. *Int J Aeroacoust* 2005; 4: 93–116.
5. Berland J, Lafon P, Crouzet F, et al. Numerical insight into sound sources of a rod-airfoil flow configuration using direct noise calculation. In: *16th AIAA/CEAS aeroacoustics conference, American institute of aeronautics and astronautics*, 2010. Reston, VA: AIAA.
6. Eltaweel A and Wang M. Numerical simulation of broadband noise from airfoil-wake interaction. *AIAA Paper* 2011; 2802: 5–8.
7. Giret J-C, Sengissen A, Moreau S, et al. Prediction of the sound generated by a rod-airfoil configuration using a compressible unstructured les solver and a FW-H analogy. *AIAA Paper* 2012; 2058: 4–6.
8. Giret J-C, Sengissen A, Moreau S, et al. Noise source analysis of a rod-airfoil configuration using unstructured large-eddy simulation. *AIAA J* 2014; 53: 1062–1077.
9. Williams JF and Hawkings DL. Sound generation by turbulence and surfaces in arbitrary motion. *Philos Trans R Soc Lond A Math Phys Sci* 1969; 264: 321–342.
10. Jiang Y, Mao M-L, Deng XG, et al. Numerical investigation on body-wake flow interaction over rod–airfoil configuration. *J Fluid Mech* 2015; 779: 1–35.
11. Amiet R. Acoustic radiation from an airfoil in a turbulent stream. *J Sound Vib* 1975; 41: 407–420.
12. Seo JH and Moon YJ. Aerodynamic noise prediction for long-span bodies. *J Sound Vib* 2007; 306: 564–579.
13. Roger M, Schram C and De Santana L. Reduction of airfoil turbulence-impingement noise by means of leading-edge serrations and/or porous materials. In: *19th AIAA/CEAS aeroacoustics conference*, Berlin, 2013. Reston, VA: AIAA.
14. Clair V, Polacsek C, Le Garrec T, et al. Experimental and numerical investigation of turbulence-airfoil noise reduction using wavy edges. *AIAA J* 2013; 51: 2695–2713.
15. Chen W, Qiao W, Wang L, et al. Rod-airfoil interaction noise reduction using leading edge serrations. In: *21st AIAA/CEAS aeroacoustics conference*, Dallas, TX, p. 3264. Reston, VA: AIAA.

16. Kim D, Lee G-S and Cheong C. Inflow broadband noise from an isolated symmetric airfoil interacting with incident turbulence. *J Fluid Struct* 2015; 55: 428–450.
17. Narayanan S, Chaitanya P, Haeri S, et al. Airfoil noise reductions through leading edge serrations. *Phys Fluid* 2015; 27: 025109.
18. Durbin PA and Reif BP. *Statistical theory and modeling for turbulent flows*. Chichester: John Wiley & Sons, 2011.
19. Smagorinsky J. General circulation experiments with the primitive equations: I. the basic experiment. *Mon Weather Rev* 1963; 91: 99–164.
20. Issa RI. Solution of the implicitly discretised fluid flow equations by operator-splitting. *J Comput Phys* 1986; 62: 40–65.
21. Patankar SV and Spalding DB. A calculation procedure for heat, mass and momentum transfer in three-dimensional parabolic flows. *Int J Heat Mass Transf* 1972; 15: 1787–1806.
22. Welch PD. The use of fast Fourier transform for the estimation of power spectra: a method based on time averaging over short, modified periodograms. *IEEE Trans Audio Electroacoust* 1967; 15: 70–73.
23. Kato C and Ikegawa M. Large eddy simulation of unsteady turbulent wake of a circular cylinder using the finite element method. *Adv Numer Simulat Turb Flow* 2003; 1: 49–56.
24. Norberg C. Pressure forces on a circular cylinder in cross flow. In: Wakes BB (ed.) *Dynamics and instabilities*. Berlin: Springer, 1993, pp.275–278.
25. Achenbach E. Distribution of local pressure and skin friction around a circular cylinder in cross-flow up to re $= 5 \times 106$. *J Fluid Mech* 1968; 34: 625–639.
26. Sharma A, Richards SK, Wood TH, et al. Numerical prediction of exhaust fan-tone noise from high-bypass aircraft engines. *AIAA J* 2009; 47: 2866–2879.

Appendix 1

A time series analysis

Cross-correlation between two random processes which are functions of time, say $u(t)$ and $v(t)$, is defined as

$$R_{uv}(\tau) = \lim_{T\to\infty} \frac{1}{T}\int_0^T u(t)v(t+\tau)\,\mathrm{d}t \tag{10}$$

If the processes $u(t)$ and $v(t)$ correspond to time signals of a stochastic quantity (say pressure in a turbulent flow) measured at two different spatial locations $\mathbf{x}$ and $\mathbf{y}$, then the cross correlation between these two random processes is called the two-point cross correlation function of that quantity (pressure) and expressed as

$$R_{xy}(\tau) = \lim_{T\to\infty} \frac{1}{T}\int_0^T p(\mathbf{x},t)\,p(\mathbf{y},t+\tau)\,\mathrm{d}t \tag{11}$$

Cross-spectral density or cross power spectrum is defined as the Fourier transform of $R_{xy}(\tau)$ as

$$S_{xy}(\omega) = \int_{-\infty}^{\infty} R_{xy}(\tau)\ \exp(-i\omega\tau)\,\mathrm{d}\tau \tag{12}$$

If the two points $\mathbf{x}$ and $\mathbf{y}$ are identical, then the cross-correlation reduces to autocorrelation, denoted by $R_{pp}(\tau)$, and the cross-spectral density reduces to PSD. These are defined as

$$R_{pp}(\tau) = \lim_{T\to\infty} \frac{1}{T}\int_0^T p(t)\, p(t+\tau)\, \mathrm{d}t \text{ and}$$

$$S_{pp}(\omega) = \int_{-\infty}^{\infty} R_{pp}(\tau)\ \exp(-i\omega\tau)\, \mathrm{d}\tau \tag{13}$$

The Wiener–Khinchin theorem as can be used to compute PSD as

$$\begin{aligned} S_{pp}(\omega) &= E|\hat{p}(\omega)|^2 \\ &= \frac{1}{T}\int_0^T p^*(t)\exp(i\omega t)\, \mathrm{d}t \int_0^T p(t')\exp(-i\omega t')\, \mathrm{d}t' \end{aligned} \tag{14}$$

where $\hat{p}(\omega)$ is the Fourier transform of $p(t)$. PSD for a discrete series (p_n) with N points, can be obtained using

$$S_{pp}(\omega) = \frac{(\delta t)^2}{T}|\sum_{n=1}^{N} p_n \exp(-i\omega\, n\delta t)|^2 \tag{15}$$

PSD calculations are typically averaged over multiple samples to reduce the statistical scatter in the spectra.

Spatial coherence between two points **x** and **y** is defined as

$$\gamma_{xy}^2(\omega) = \frac{|S_{xy}(\omega)|^2}{S_{xx}(\omega)S_{yy}(\omega)} \tag{16}$$

where $S_{xx}(\omega)$ is $S_{pp}(\omega)$ evaluated at **x** and $S_{yy}(\omega)$ is $S_{pp}(\omega)$ evaluated at **y**.